The Ekman Streamfunction: a wind-derived metric to quantify the Southern Ocean overturning circulation

Kial Douglas Stewart[1], Andrew McC. Hogg[1], Matthew H. England[2], Darryn W. Waugh[3], and Andrew E. Kiss[4]

[1]Australian National University
[2]University of New South Wales
[3]Johns Hopkins University
[4]The Australian National University

November 24, 2022

Abstract

We introduce a novel wind-derived metric to quantify variability in the Southern Ocean overturning circulation. This metric, which we call the Ekman streamfunction, integrates the Ekman pumping vertical velocity zonally and northwards from the Antarctic coastline to a given latitude. To evaluate the relationship between the Ekman streamfunction and Southern Ocean overturning circulation, we use a global 0.1 ocean–sea-ice model driven with interannual forcing (1958-2018). Throughout much of the Southern Ocean, strong correlations (r>0.9) exist between the Ekman streamfunction and the Southern Ocean overturning circulation on monthly and annual timescales. A regression analysis identifies regions where Ekman streamfunction variability coincides with >4Sv changes in the overturning; one such location is where the wind stress curl changes sign and the Ekman pumping velocity is highly variable. This study offers a new approach to infer recent changes in the Southern Ocean overturning circulation from existing datasets of wind stress.

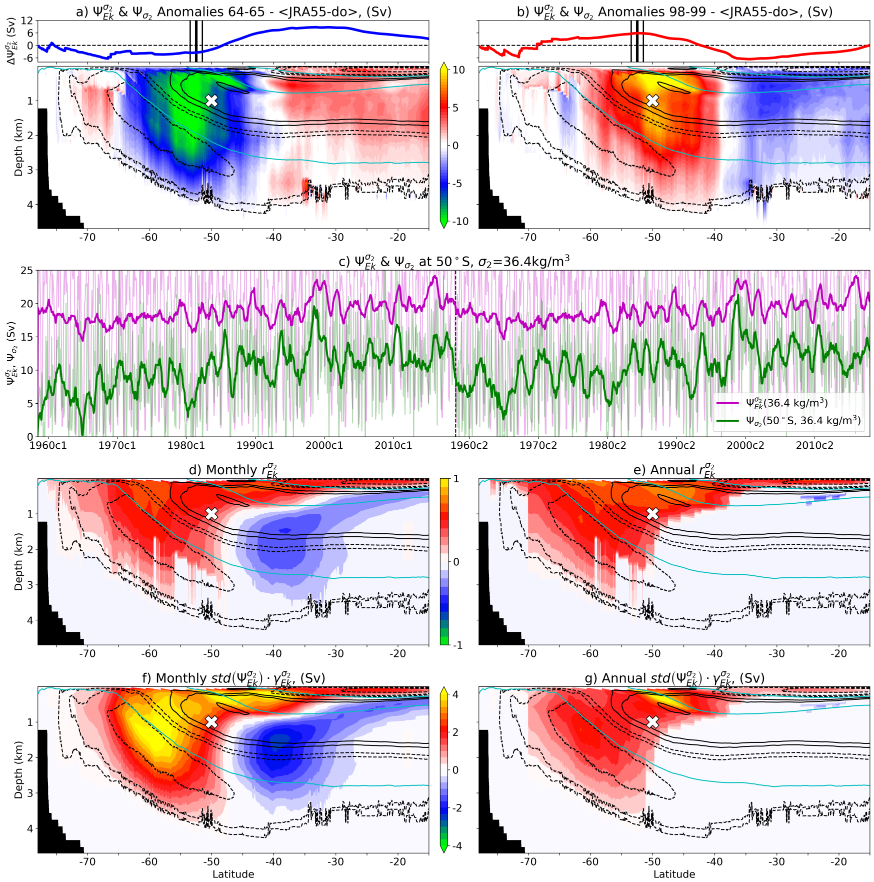

a) $\Psi_{Ek}^{\sigma_2}$ & Ψ_{σ_2} Anomalies 64-65 - <JRA55-do>, (Sv)
b) $\Psi_{Ek}^{\sigma_2}$ & Ψ_{σ_2} Anomalies 98-99 - <JRA55-do>, (Sv)
$\Delta\Psi_{Ek}^{\sigma_2}$ (Sv)
Depth (km)
c) $\Psi_{Ek}^{\sigma_2}$ & Ψ_{σ_2} at 50°S, σ_2=36.4kg/m^3
$\Psi_{Ek}^{\sigma_2}$, Ψ_{σ_2} (Sv)
$\Psi_{Ek}^{\sigma_2}$(36.4 kg/m^3)
Ψ_{σ_2}(50°S, 36.4 kg/m^3)
1960c1 1970c1 1980c1 1990c1 2000c1 2010c1 1960c2 1970c2 1980c2 1990c2 2000c2 2010c2
d) Monthly $r_{Ek}^{\sigma_2}$
e) Annual $r_{Ek}^{\sigma_2}$
f) Monthly $std(\Psi_{Ek}^{\sigma_2}) \cdot \gamma_{Ek}^{\sigma_2}$, (Sv)
g) Annual $std(\Psi_{Ek}^{\sigma_2}) \cdot \gamma_{Ek}^{\sigma_2}$, (Sv)
Latitude

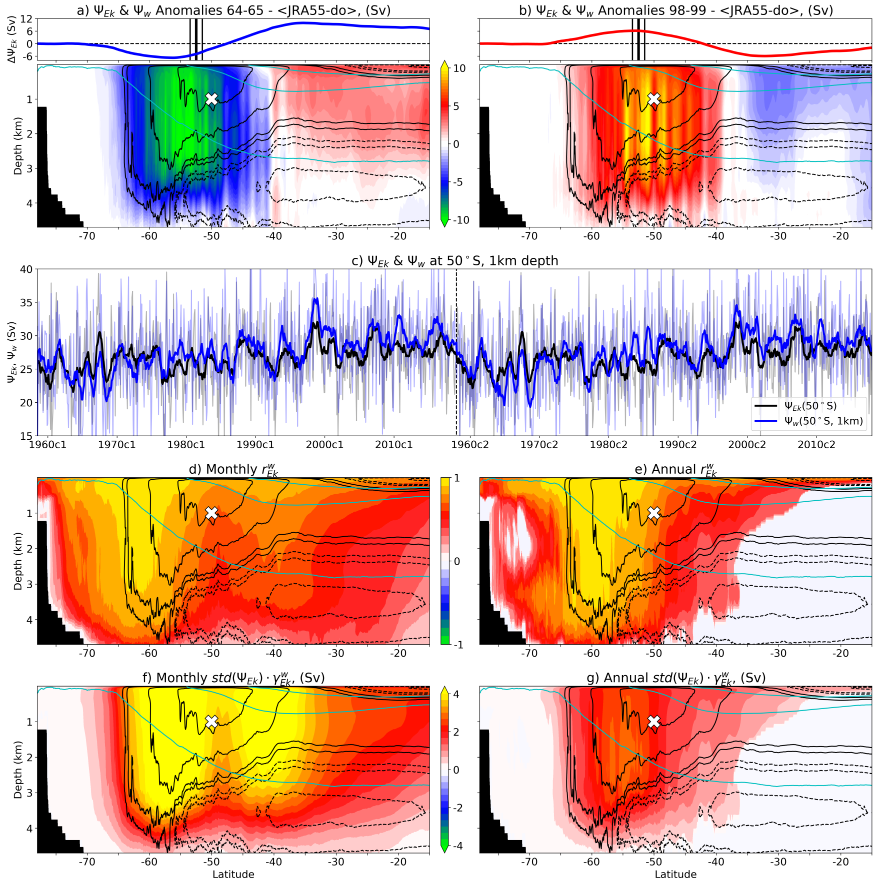
a) Ψ_{Ek} & Ψ_w Anomalies 64-65 - <JRA55-do>, (Sv)
b) Ψ_{Ek} & Ψ_w Anomalies 98-99 - <JRA55-do>, (Sv)
$\Delta\Psi_{Ek}$ (Sv)
Depth (km)
c) Ψ_{Ek} & Ψ_w at 50°S, 1km depth
Ψ_{Ek}, Ψ_w (Sv)
Ψ_{Ek}(50°S)
Ψ_w(50°S, 1km)
1960c1
1970c1
1980c1
1990c1
2000c1
2010c1
1960c2
1970c2
1980c2
1990c2
2000c2
2010c2
d) Monthly r^w_{Ek}
e) Annual r^w_{Ek}
f) Monthly $std(\Psi_{Ek}) \cdot \gamma^w_{Ek}$, (Sv)
g) Annual $std(\Psi_{Ek}) \cdot \gamma^w_{Ek}$, (Sv)
Latitude

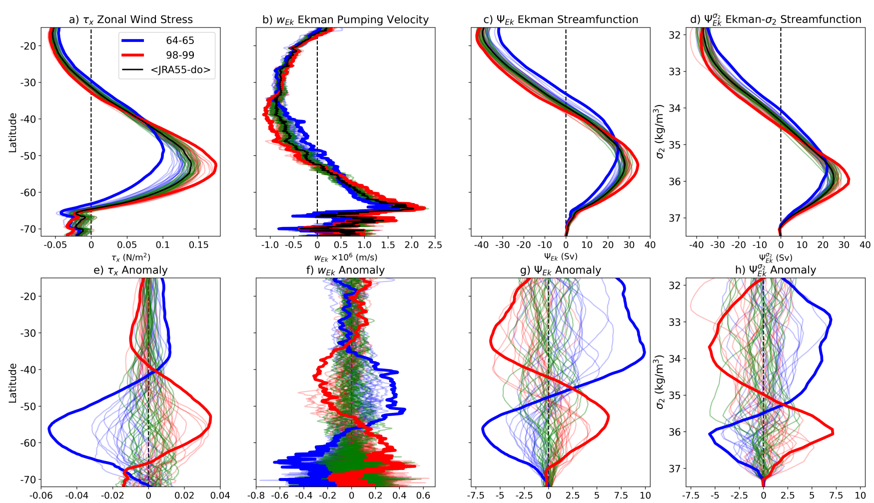
a) τ_x Zonal Wind Stress
b) w_{Ek} Ekman Pumping Velocity
c) Ψ_{Ek} Ekman Streamfunction
d) $\Psi^{\sigma_2}_{Ek}$ Ekman-σ_2 Streamfunction
64-65
98-99
<JRA55-do>
Latitude
σ_2 (kg/m^3)
τ_x (N/m^2)
w_{Ek} $\times 10^6$ (m/s)
Ψ_{Ek} (Sv)
$\Psi^{\sigma_2}_{Ek}$ (Sv)
e) τ_x Anomaly
f) w_{Ek} Anomaly
g) Ψ_{Ek} Anomaly
h) $\Psi^{\sigma_2}_{Ek}$ Anomaly
$\Delta\tau_x$ (N/m^2)
Δw_{Ek} $\times 10^6$ (m/s)
$\Delta\Psi_{Ek}$ (Sv)
$\Delta\Psi^{\sigma_2}_{Ek}$ (Sv)

The Ekman Streamfunction: a wind-derived metric to quantify the Southern Ocean overturning circulation

K.D. Stewart[1], A.McC. Hogg[1,2], M.H. England[2,3], D.W. Waugh[4,5], and A.E. Kiss[1]

[1]Research School of Earth Sciences, Australian National University, Canberra, Australia
[2]Australian Research Council Centre of Excellence for Climate Extremes
[3]Climate Change Research Centre, University of New South Wales, Sydney, Australia
[4]Department of Earth and Planetary Sciences, The Johns Hopkins University, Baltimore, USA
[5]School of Mathematics and Statistics, University of New South Wales, Sydney, Australia

Key Points:

- We introduce the Ekman streamfunction as a wind-derived metric for the Southern Ocean overturning circulation.
- The Ekman streamfunction and Southern Ocean overturning circulation exhibit striking similarities, with correlations exceeding 0.9.
- Where the wind stress curl changes sign, Ekman streamfunction variability coincides with > 4Sv changes in the overturning circulation.

Corresponding author: K.D. Stewart, `kial.stewart@anu.edu.au`

Abstract

We introduce a novel wind-derived metric to quantify variability in the Southern Ocean overturning circulation. This metric, which we call the Ekman streamfunction, integrates the Ekman pumping vertical velocity zonally and northwards from the Antarctic coastline to a given latitude. To evaluate the relationship between the Ekman streamfunction and Southern Ocean overturning circulation, we use a global 0.1° ocean–sea-ice model driven with interannual forcing (1958–2018). Throughout much of the Southern Ocean, strong correlations ($r > 0.9$) exist between the Ekman streamfunction and the Southern Ocean overturning circulation on monthly and annual timescales. A regression analysis identifies regions where Ekman streamfunction variability coincides with $> 4\,\mathrm{Sv}$ changes in the overturning; one such location is where the wind stress curl changes sign and the Ekman pumping velocity is highly variable. This study offers a new approach to infer recent changes in the Southern Ocean overturning circulation from existing datasets of wind stress.

Plain Language Summary

The global ocean overturning circulation is the planetary-scale movement of waters in the vertical and north-south directions. It is the principal mechanism by which the oceans absorb, sink, and redistribute heat and carbon from the atmosphere, thereby regulating Earth's climate. Despite its importance, it is impossible to observe directly, and must be inferred from sparse and infrequent proxy measurements. The main upward branches of the overturning circulation are located in the Southern Ocean, where strong westerly winds upwell waters from below. Thus, changes in these westerly winds will lead to changes in the overturning circulation, and, subsequently, Earth's climate. Here we introduce a new tool, called the Ekman streamfunction, to analyse the change of the winds in a framework that is directly comparable with the overturning circulation. We test the Ekman streamfunction with a state-of-the-art global ocean–sea-ice model in which the overturning circulation is measured directly. We find throughout much of the Southern Ocean, the Ekman streamfunction provides a robust indicator of the strength and variability of the overturning circulation, with exceptionally high correlation. Our new tool provides a novel approach for reexamining existing datasets of winds measured from satellites, to infer recent changes in the overturning circulation.

1 Introduction

The role that the global oceans play in Earth's climate is governed by the Southern Ocean and its overturning circulation (Sallèe, 2018). The Southern Ocean overturning circulation (SOOC) maintains the bulk stratification of the global oceans through the replenishment of abyssal, deep and mode waters in all major ocean basins (J. Marshall & Speer, 2012). The SOOC is the primary process by which the oceans sequester excess heat and carbon from the atmosphere, thereby regulating climate conditions globally (Sabine et al., 2004; Roemmich et al., 2015). Thus, changes in the SOOC, anthropogenic or otherwise, will have substantial ramifications for the trajectory of Earth's climate. Quantifying the magnitude of the SOOC and its variability, however, remains a challenge; direct observation of the overturning circulation is not possible, and the few proxy measurements of the SOOC are infrequent, sparse, and with large uncertainties. Any scientific developments that grant insight into the SOOC and its dynamics are most welcome.

The SOOC, along with the global meridional overturning circulation, is the result of a complicated interplay between surface buoyancy forces, wind stress, and turbulent mixing, the effects of which, in turn, depend on one another (J. Marshall & Speer, 2012). This intrinsically-coupled nature of the SOOC forcings makes it impossible to decompose the overturning into its separate buoyancy-driven, wind-driven and mixing-driven components. Nevertheless, it is both possible and illuminating to diagnose and consider the effects of relative changes in the distinct forces that drive the SOOC, especially since these forces have recently exhibited trends. For example, the midlatitude westerly winds over the Southern Ocean, often characterised by the Southern Annular Mode (SAM) index, have strengthen and shifted poleward during the recent decades (e.g., Goyal et al., 2021). The oceanographic consequences of these trends in the Southern Hemisphere winds have received much attention of late, especially in regards to the response of the SOOC.

The scientific approaches to examining the SOOC response to changing winds are varied, but can be broadly partitioned into two distinct methodologies; the first being when the wind forcing (the independent variable of interest) is an uncontrolled variable of the system, and the second being when the wind forcing is prescribed. The first methodology typically employs coupled climate models, reanalysis products, and/or satellite- and Argo-based observations, often using statistical techniques to ascribe changes in the ocean state to changes in the wind forcing, usually represented by the SAM index (e.g., Sen Gupta & England, 2006; Sallèe et al., 2010). The second approach, which prescribes the wind forcing, typically examines simulations in either idealised domains (e.g., Abernathey et al., 2011), or oceanographically-realistic domains that are driven with wind forcing derived from reanalysis products (e.g., Farneti et al., 2015). For either methodology, the results are usually presented in a form that relates the relative changes in SOOC transport (in Sverdrups, Sv; where $1\,\mathrm{Sv} = 10^6\,\mathrm{m^3/s}$) to relative changes in the wind stress ($\mathrm{N/m^2}$). While this presentation may be sufficient for ascertaining the general sensitivity of the SOOC response to bulk variations of the wind stress, the open dimensional divide between these two quantities begs the question: Is there a better way to more directly relate the Southern Ocean overturning circulation to wind stress?

Here we bridge this dimensional divide by casting the wind stress in terms of a streamfunction, which we call the Ekman streamfunction, introduced in §2. The Ekman streamfunction is developed from the vertical velocities associated with the Ekman pumping, which are derived from the curl of the wind stress. This Ekman streamfunction is a metric that theoretically quantifies the mechanical forcing of the winds on the SOOC; it does not incorporate the wind-driven buoyancy or mixing components. In §3, we detail the high-resolution global ocean–sea-ice model, which we use to evaluate the relationship between the Ekman streamfunction and the SOOC. We present and discuss our findings in §4, and summarise our conclusions in §5.

2 Theory

The SOOC can be characterised in terms of its Eulerian streamfunction in latitude–depth space, and its residual streamfunction in latitude–potential density space (e.g., Zika et al., 2012). The local cartesian coordinates for the zonal, meridional and vertical directions are given by x, y and z (m), respectively, with the potential density as σ_2 ($\mathrm{kg/m^3}$), which is the potential density of seawater referenced to 2000 dbar less $1000\,\mathrm{kg/m^3}$. The Eulerian streamfunction can be developed by integrating the vertical velocity w (m/s) in both the zonal direction and in the meridional direction from a southern latitude corresponding to y_1 (where y_1 is at a circle of latitude located entirely inside the Antarctic continent) northwards to a given latitude corresponding to y;

$$\Psi_w\left(y, z, t\right) = \int \int_{y_1}^{y} w\left(x, y', z, t\right) dy' dx. \tag{1}$$

The Eulerian streamfunction is usually defined in terms of the meridional velocity, v, integrated in both the zonal direction and vertically from the ocean bottom to a given depth; however, the definition in Equation (1) is mathematically equivalent and has a more direct application to our subsequent analysis.

In a similar manner, the residual streamfunction is developed by integrating the meridional velocity, v, in both the zonal direction and vertically from the bottom of the ocean upwards to a depth z where the potential density reaches a given value σ_2 (assuming a stable stratification);

$$\Psi_{\sigma_2}(y, \sigma_2, t) = \int\int_{\sigma_2{}' > \sigma_2} v(x, y, z, t)\, dz dx. \tag{2}$$

Compared to the Eulerian streamfunction, the residual streamfunction is more important for Earth's climate as it represents the meridional exchanges of water properties in potential density space (e.g., Zika et al., 2012).

By taking the curl of the wind stress $\boldsymbol{\tau}$ (N/m^2), the vertical velocity associated with Ekman pumping w_{Ek} (m/s) at the base of the surface Ekman layer is estimated as

$$w_{Ek}(x, y, t) = \nabla \times \left(\frac{\boldsymbol{\tau}(x, y, t)}{\rho_0 f(y)} \right), \tag{3}$$

where, ρ_0 is the reference seawater density and $f(y)$ is the local Coriolis parameter. In this approximation, w_{Ek} is a wind-derived metric that should be considered a theoretical estimate of the actual vertical velocities; for instance, it does not account for vertical velocities arising from buoyancy-driven convection. Importantly, however, estimates of $\boldsymbol{\tau}$, and thus w_{Ek}, are obtainable from satellite-derived global datasets of wind stress.

Following the approach in Equation (1), where the model-diagnosed vertical velocity w is used to develop the Eulerian streamfunction, we take the Ekman pumping velocity w_{Ek} and integrate it zonally and meridionally in a similar fashion,

$$\Psi_{Ek}(y, t) = \int\int_{y_1}^{y} w_{Ek}(x, y', t)\, dy' dx. \tag{4}$$

We call Ψ_{Ek} the Ekman streamfunction. By this definition, Ψ_{Ek} can be thought of as an estimate of the Eulerian overturning circulation at the base of the surface Ekman layer due to Ekman pumping. Developing the Ekman streamfunction with the Ekman pumping vertical velocities is mathematically equivalent to using the meridional Ekman transport (which can be estimated from the latitudinal distribution of zonal wind stress τ_x), but has the advantage that it does not require assumptions to be made about the vertical structure of the Ekman-driven flows (e.g., Gray & Riser, 2014; Tandon et al., 2020).

The Ekman streamfunction can be further extended from latitude space into potential density space by integrating w_{Ek} in both the zonal and meridional directions where the surface potential density is greater than a given value of σ_2;

$$\Psi_{Ek}^{\sigma_2}(\sigma_2, t) = \int\int w_{Ek}(x, y, t)\, \mathrm{H}(\sigma_2{}' - \sigma_2)\, dy dx, \tag{5}$$

where H is the Heaviside step function, and the superscript σ_2 denotes $\Psi_{Ek}^{\sigma_2}$ is in surface σ_2-space. Note that in this instance, σ_2 serves as a pseudo-meridional coordinate as the surface potential density approximately scales with latitude. We call $\Psi_{Ek}^{\sigma_2}$ the Ekman streamfunction in density coordinates.

3 Model & Methodology

We employ the 0.1° configuration of the Australian Community Climate and Earth System Simulator ocean model version 2 (ACCESS-OM2-01; updated from Kiss et al., 2020), the flagship ocean–sea-ice model of the Consortium for Ocean–Sea-Ice Modelling in Australia (COSIMA). The ACCESS-OM2-01 simulation is initialised with January temperature and salinity fields from the World Ocean Atlas 2013 v2 monthly climatology (WOA13; Locarnini et al., 2013; Zweng et al., 2013), and forced with prescribed atmospheric conditions taken from the Japanese atmospheric reanalysis dataset for driving ocean models (JRA55-do v1.4; Tsujino et al., 2018). These prescribed atmospheric conditions are the interannual forcing (JRA55-do-IAF) that runs 61 years from 1958 to 2018, inclusive. Two cycles of the JRA55-do-IAF are imposed in serial, such that in the second cycle there is a sudden transition at the end of 31st December 2018 back to the start of 1st January 1958, as per the forcing protocol of Ocean Model Intercomparison Project phase 2 (OMIP2; Tsujino et al., 2020).

We analyse monthly means to evaluate the two overturning streamfunctions and the two Ekman streamfunctions, as detailed in §2. Due to the dominance of the seasonal signal in these terms, it is necessary to first de-season the monthly mean output by removing the average of the entire two JRA55-do-IAF cycles of a given month from that given month (i.e., the average state of the 122 Januarys is removed from each January, and so on, for each of the 12 months). Our analysis then focusses on the comparison of the four streamfunctions at two temporal scales: (1) the de-seasoned monthly means, and (2) the 12-month running averages.

To quantify the relationships between the streamfunctions, we calculate the respective correlation coefficients, r, between the timeseries of the Ekman streamfunctions and the overturning streamfunctions at zero lag. Considering the high degree of autocorrelation in these streamfunctions, it is necessary to perform a statistical significance test that uses an effective sample size N_{eff}, given by

$$N_{eff} = N\left(\frac{1 - r_1 r_2}{1 + r_1 r_2}\right), \tag{6}$$

where N is the actual sample size ($N = 1464$ months), and r_1 and r_2 are the lag-1 autocorrelations of the two timeseries of interest (e.g. see Santer et al., 2000). Note that the effective sample size N_{eff} varies spatially, and as a significance test we identify and reject regions where $|r\sqrt{N_{eff}}| > 2$, which corresponds to the correlation being significant at the 95% level.

We also perform the following linear regression analyses:

$$\Psi_w\left(y, z, t\right) = \gamma^w_{Ek}\left(y, z\right)\Psi_{Ek}\left(y, t\right) + c_1, \tag{7}$$

and,

$$\Psi_{\sigma_2}\left(y, \sigma_2, t\right) = \gamma^{\sigma_2}_{Ek}\left(y, \sigma_2\right)\Psi^{\sigma_2}_{Ek}\left(\sigma_2, t\right) + c_2, \tag{8}$$

where the regression coefficients γ^w_{Ek} and $\gamma^{\sigma_2}_{Ek}$ represent the change in overturning streamfunctions coincident with unit changes in Ekman streamfunctions.

The correlation and regression analyses are performed on the de-seasoned monthly means and 12-month running averages of the streamfunctions for the entire two JRA55-do-IAF cycles of the ACCESS-OM2-01 simulation, returning distributions of correlations and linear regression coefficients in latitude–depth and latitude–potential density space. For the regression analysis, in order to better gauge the magnitude of the overturning circulation anomalies indicated by the coefficients $\gamma^w_{Ek}\left(y, z\right)$ and $\gamma^{\sigma_2}_{Ek}\left(y, \sigma_2\right)$, we scale them by the standard deviations of the respective Ekman streamfunctions $std\left(\Psi_{Ek}\left(y\right)\right)$ and $std\left(\Psi^{\sigma_2}_{Ek}\left(\sigma_2\right)\right)$. These scaled regression coefficients $std\left(\Psi_{Ek}\right)\cdot\gamma^w_{Ek}$ and $std\left(\Psi^{\sigma_2}_{Ek}\right)\cdot\gamma^{\sigma_2}_{Ek}$ thus represent the magnitude of the change in overturning streamfunctions, in Sverdrups, that is coincident with a one standard deviation change in the Ekman streamfunction.

4 Results & Discussion

The zonal means of the July–June averages of zonal wind stress τ_x highlights the considerable variability in both the latitude of the peak wind stress (48–54°S), and its magnitude (0.9–0.17N/m^2), with periods of weaker forcing conditions (blue lines) tending to peak relatively further north (Fig. 1a). This range of variability in both the latitude and magnitude of the peak zonal wind stress is consistent with previous analysis

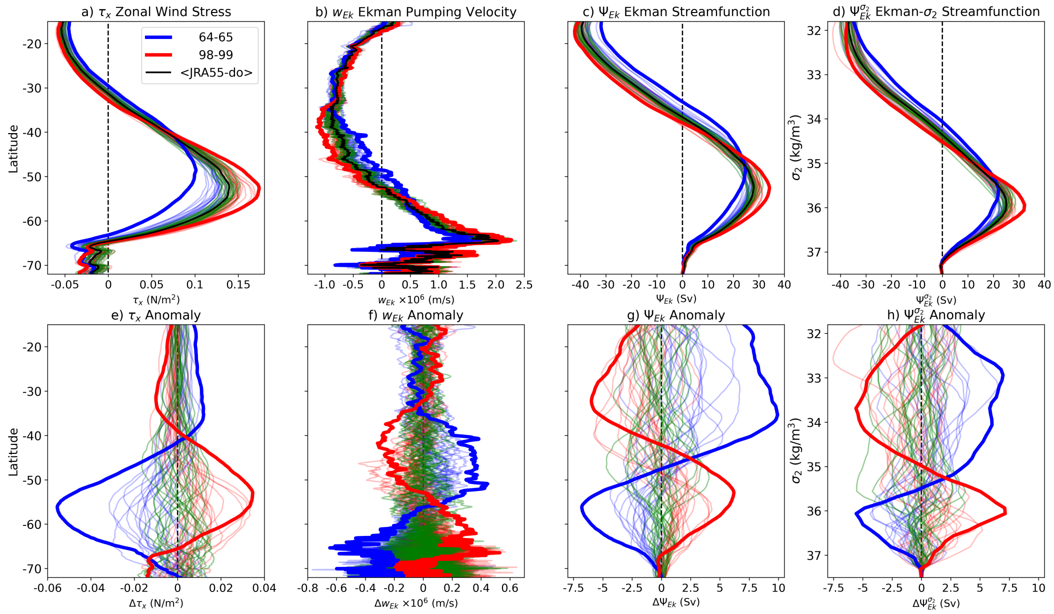

Figure 1. Zonal means of the July–June averages for the (a) zonal wind stress, (b) Ekman pumping velocity, (c) Ekman streamfunction, all calculated from the second cycle of the JRA55-do-IAF, along with their respective anomalies from the cycle mean (e-g). The thicker blue and red lines denote two end-member cases of extreme weak and strong wind forcing, corresponding to July 1964 – June 1965 (64-65) and July 1998 – June 1999 (98-99), respectively, with the black lines showing the mean of the second JRA55-do-IAF cycle (<JRA55-do>). The faint lines are included to be indicative of the extent of variability in these fields; these are coloured blue, green and red, indicating weak, neutral and strong forcing conditions, respectively. Equivalent depictions of the (d) Ekman streamfunction in density coordinates, and its (h) anomaly, plotted as a function of the outcropping potential density σ_2.

of reanalyses and models (e.g., Swart & Fyfe, 2012). Using the 61-year average of second JRA55-do-IAF cycle as a reference (referred to as <JRA55-do>), the peaks in the zonal wind stress anomalies also exhibit considerable variability, with typical magnitudes of ±25% (±0.03N/m^2) of the average zonal wind stress, and more than 40% decrease for the period July 1964 to June 1965 (64-65; Fig. 1e).

The Ekman pumping velocities also exhibit considerable interannual variability in their magnitude and latitudinal distribution (Fig. 1b). Here, negative w_{Ek} arises when there is a convergence of surface waters, reflecting a downward motion of water driven by the wind stress, with positive w_{Ek} indicating upwelling; these are often referred to as Ekman pumping and Ekman suction, respectively. The interannual variability of the zero-crossing latitude of w_{Ek}, which approximately corresponds to the latitude of peak τ_x, indicates that these latitudes (48–54°S) can experience both upwelling and downwelling on a year-to-year basis and thus are likely to exhibit substantial variability in their hydrographic properties. Strong forcing conditions (red lines) are associated with an enhancement of both upwelling and downwelling velocities. The Ekman pumping velocity anomalies are largest in regions prone to seasonal sea-ice (south of 65°S); north of the sea-ice, the interannual anomalies span $\pm 0.4\times 10^{-6}$m/s, which for some latitudes (∼45–60°S) can be larger than the average w_{Ek} velocity (Fig. 1f).

The Ekman streamfunction (Eqn. 4) peaks between ∼27–35 Sv centered around 50°S, where w_{Ek} changes sign (Fig. 1c). The two end-member cases of weak and strong wind forcing envelop the range of Ekman streamfunctions from the second cycle of JRA55-do-IAF. Note that while this new field is developed from the comparatively noisy Ekman pumping velocity w_{Ek}, being a double area integral the Ekman streamfunction is smooth and well-behaved; this is particularly the case for the seasonal sea-ice regions where the substantial variability of the Ekman pumping velocity is muted by its relatively small areal extent. The Ekman streamfunction anomalies (Fig. 1g) span the range -7 to +10 Sv; strong forcing conditions tend to have positive anomalies to the south of ∼50°S, and negative anomalies to the north, which is mirrored for weak forcing conditions.

There are similarities between the distributions and magnitudes of the two Ekman streamfunctions (Fig. 1c,d); they both initially increase towards northern/lighter outcropping waters, with the Ekman streamfunction in density coordinates peaking between ∼22–33 Sv around $\sigma_2 = 35.8$kg/m^3. The similar distributions of the Ekman streamfunctions here demonstrates the close relationship between latitude and outcrop potential density on an annual timescale, and extend to the anomalies of the Ekman streamfunction in density coordinates (Fig. 1h).

To examine the relationship between the Ekman streamfunction and the model-diagnosed Southern Ocean overturning circulation, we first focus on the Eulerian case (Fig. 2). The Eulerian streamfunction anomalies primarily depend on latitude, and are consistent with the Ekman streamfunction anomalies (overlying sub-panels of Fig. 2a,b) in both latitudinal distribution and magnitude but with some differences: the magnitude of the anomalous Ekman streamfunction is weaker (stronger) than the Eulerian streamfunction in the south (north), and the latitude of the Ekman streamfunction zero anomaly is displaced south. The strong, vertically-coherent, latitudinal dependence reflects the rapid and deep penetrating response of the Southern Ocean circulation to variations in the wind stress.

Timeseries of the Eulerian and Ekman streamfunctions at a given location further demonstrate their close resemblance and offer an indication of their relative magnitudes and behaviours (Fig. 2c). At 50°S and 1 km depth, the 12-month running averages of the Eulerian and Ekman streamfunctions are of similar magnitude, and with a correlation of $r^w_{Ek} = 0.78$. Note that this close agreement in magnitude is not necessarily representative of other locations throughout the Southern Ocean. Interestingly, both cycles of the JRA55-do-IAF exhibit a long-term trend in the streamfunctions from a minimum

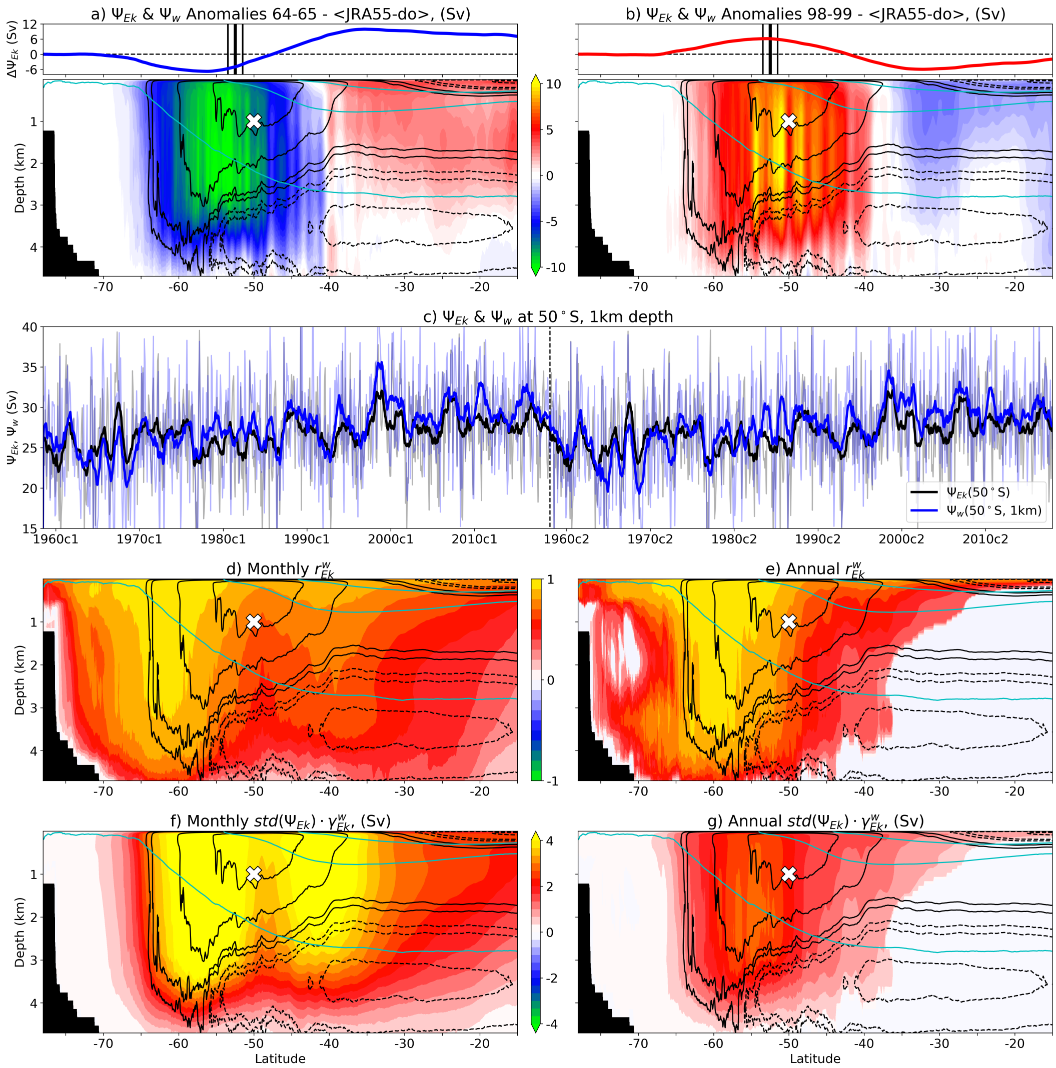

Figure 2. The Eulerian streamfunction anomalies (colour shaded) for the periods (a) July 1964 – June 1965 and (b) July 1998 – June 1999, relative to the mean of the second cycle of JRA55-do-IAF, with their respective Ekman streamfunction anomalies included for reference (lines in upper panels). The <JRA55-do> mean Eulerian streamfunction is contoured in black at ±2.5, 5, 15, 25 Sv intervals with the circulation going clockwise (anticlockwise) around the solid (dashed) contours. The σ_2=35, 36, 37 kg/m^3 isopycnals of <JRA55-do> are shown in cyan. The black lines in the upper panels indicate the latitudinal location of the <JRA55-do> Ekman streamfunction maximum (thick) and its annual standard deviation (thin). Panel (c) presents timeseries over both cycles (separated by the vertical dashed line) of the Eulerian and Ekman streamfunctions at 50°S and 1 km depth; this location is denoted by the white crosses in the other panels. The bold lines are the 12-month running averages; faint lines are the monthly means included so as to be indicative of the intra-annual variability. Distributions of the statistically significant correlation coefficients r^w_{Ek} and the scaled regression coefficients $std(\Psi_{Ek}) \cdot \gamma^w_{Ek}$ calculated from the (d,f) de-seasoned monthly means and (e,g) 12-month running averages. The black and cyan contours, and the white crosses, are the same as for panels a,b.

around 1964-65 to a maximum around 1998-99 (which happen to coincide with the two extreme end-member periods), where the streamfunctions increase by approximately 8 Sv each (equivalent to 2.3 Sv/decade); this long-term trend is consistent with that of the observation-based SAM index (G. Marshall, 2003).

To understand the extent to which this strong relationship extends throughout the Southern Ocean, we examine the distribution of r^w_{Ek}. On the monthly timescale, there is a high correlation ($r^w_{Ek} > 0.5$) down to 4 km depth and north to 20°S (Fig. 2d). The region between 65–55°S exhibits the strongest correlation ($r^w_{Ek} > 0.9$), with a second, relatively weaker local maxima of $r^w_{Ek} > 0.7$ apparent between 45–35°S and reaching 2 km depth. The strong correlations at zero lag in these regions reflect the rapid response of the Eulerian streamfunction to the wind-driven variability, which is evidently being captured by the Ekman streamfunction.

Widening the temporal scale to the 12-month running averages has the effect of reducing the strength of the correlation north of 50°S, and increasing it between 65–50°S (Fig. 2e). The region with the strongest correlation of $r^w_{Ek} > 0.7$, between 65–50°S and down to 4 km depth, corresponds to the upwelling flank of the "Deacon cell", a localized wind-driven overturning of waters in Eulerian space with near-uniform properties such that it does not contribute to the meridional transport of tracer (e.g., Zika et al., 2012; Farneti et al., 2015). The regions with statistically significant correlations shallows from 4.5 km deep at around 50°S to 500 m depth at 25°S; north of this, the regions of significance are confined to the surface waters only.

To understand the relative magnitudes of the Eulerian and Ekman streamfunction covariances, we examine the scaled regression coefficient $std\,(\Psi_{Ek})\cdot\gamma^w_{Ek}$, which is indicative of the magnitudes of Eulerian streamfunction anomaly (in Sverdrups) that occur coincident with one standard deviation change in the Ekman streamfunction. For the de-seasoned monthly means, the scaled regression distribution is greater than 2 Sv north of the seasonal sea-ice regions (65°S) and down to a depth of 4 km, with two distinct maxima of over 4 Sv centered at 57°S and 40°S (Fig. 2f). These two maxima coincide with the up- and downwelling branches of the Deacon cell, evident by the closed circulation contours of the Eulerian streamfunction. The magnitude of the scaled regression decreases as the temporal scale is widened to the 12-month running average (Fig. 2g), in part due to the reduction in the standard deviation of the longer-term averaged Ekman streamfunction. The maximum annual scaled regression occurs between 60–50°S and down to 4 km depth, and in places reaching over 3 Sv. The northern maximum around 40°S in the de-seasoned monthly means is not evident in the longer temporal average. As with the equivalent correlation distribution (Fig. 2e), the strongest positive region corresponds to the upwelling branch of the Deacon cell, reflecting the ability of the Ekman streamfunction to represent the effect of wind stress variability on this wind-driven circulation feature.

While the correlations between the Eulerian and Ekman streamfunctions are both strong and deep-reaching, the Eulerian overturning circulation does not necessarily correspond to property transports, especially in the Southern Ocean (Zika et al., 2012). The residual streamfunction, in contrast, represents the meridional exchanges of water masses in potential density space, and is substantially more important for Earth's climate. While the traditional coordinates of the residual streamfunction span latitude–potential density space, for ease of comparison with the Eulerian streamfunction here we interpolate the residual streamfunction into latitude–depth space, and the Ekman streamfunction in density coordinates into latitude space (Fig. 3a,b). Note that these interpolations are for the purposes of plotting only; the following correlation and regression analyses are performed in latitude–potential density space. The magnitude and distribution of the residual streamfunction anomaly fields are largely consistent with those of the Ekman streamfunction anomalies, especially between 60–40°S. The strong, vertically-coherent latitudinal dependence of the residual streamfunction anomaly distributions, which is

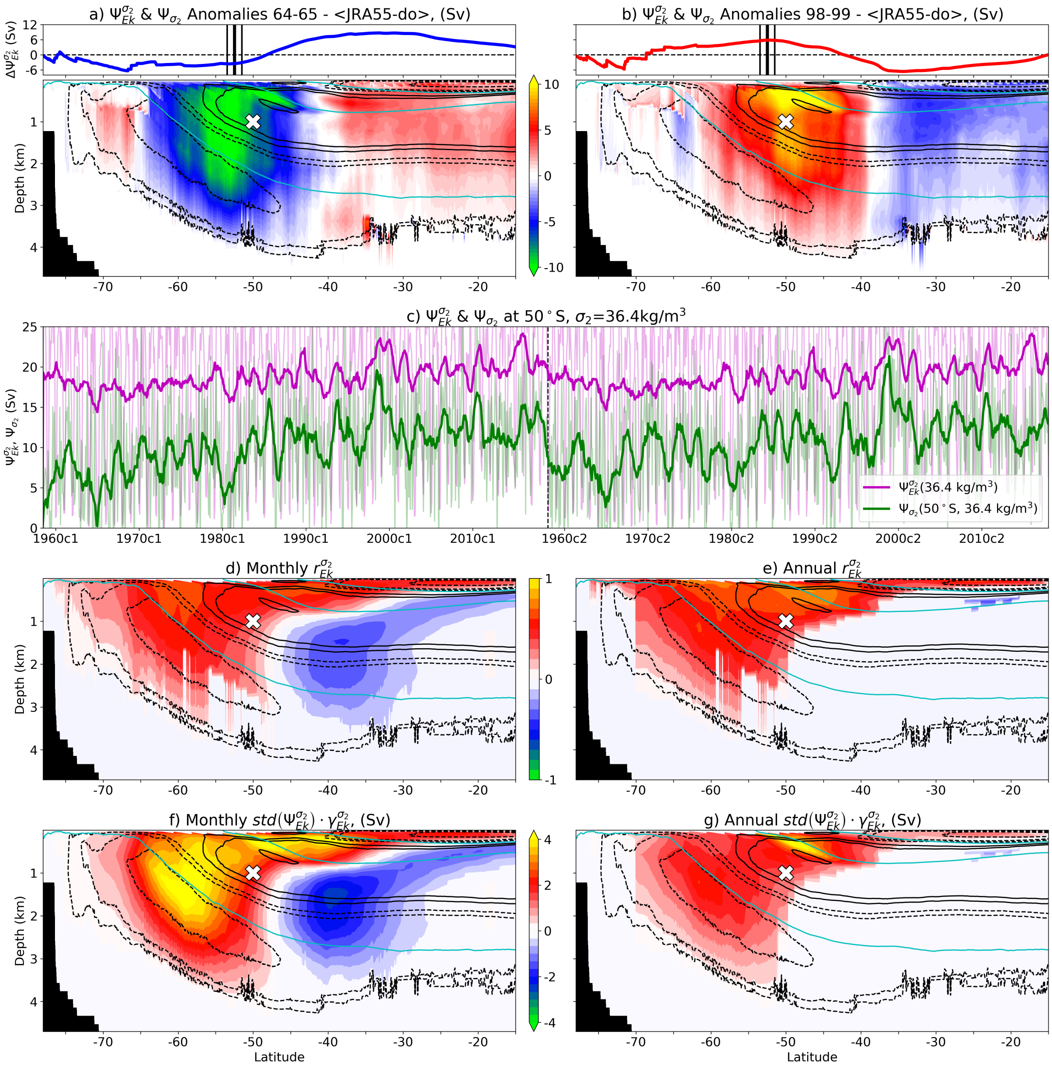

Figure 3. As for Figure 2, only showing the residual streamfunction anomalies (colour shaded) with their respective anomalies of the Ekman streamfunction in density coordinates (upper panels) for reference. Panel (c) presents timeseries of the residual and Ekman streamfunctions at 50°S and $\sigma_2 = 36.4\,\text{kg/m}^3$ (white crosses in other panels). Panels (d,e) show the distributions of the statistically significant correlation coefficients $r_{Ek}^{\sigma_2}$ for the de-seasoned monthly means and 12-month running averages, respectively, and panels (f,g) show their scaled regression coefficients $std\,(\Psi_{Ek}^{\sigma_2}) \cdot \gamma_{Ek}^{\sigma_2}$. To facilitate comparison with Figure 2, the residual and Ekman streamfunctions in density coordinates have been interpolated into latitude–depth space.

also present in the Eulerian streamfunction anomaly distributions (Fig. 2a,b), again reflects the rapid and deep response of the Southern Ocean to variations in the wind forcing. In the vicinity of the outcrop of $\sigma_2 = 36\text{kg/m}^3$, which is at approximately 52°S and coincides with the change of sign of the wind stress curl, there is evidence of the residual streamfunction anomaly signal penetrating from the surface into the interior along isopycnals (i.e., aligned with the cyan contours) and reaching northwards of 45°S.

As for the Eulerian case, we select a location in latitude–potential density space (50°S and $\sigma_2 = 36.4\text{kg/m}^3$) and present the timeseries of the residual and Ekman streamfunctions in density coordinates (Fig. 3c). At this location, the Ekman streamfunction is always larger than the residual streamfunction, which initially starts at rest. The correlation between the residual and Ekman streamfunctions at this location is $r_{Ek}^{\sigma_2} = 0.64$, which is slightly weaker than that of the Eulerian and Ekman streamfunctions ($r_{Ek}^{w} = 0.78$; Fig. 2c); this reflects the different processes by which the wind stress variability signal propagates through the Eulerian and residual overturning circulations. That is, in the Eulerian case the wind variability signal propagates vertically into the ocean via the barotropic mode, tending to have a near immediate and full-depth response; in the residual case, the wind variability signal propagates into the interior along isopycnals, which tends to be a slower process. Note that while the long-term trend that was evident in the Eulerian case between 1964-65 and 1998-99 is also present here, the trend appears relatively weaker for the Ekman streamfunction in density coordinates ($\sim$5 Sv) and relatively stronger for the residual streamfunction ($\sim$11 Sv).

The distribution of the statistically significant correlations between the de-seasoned monthly means of the residual and Ekman streamfunctions in density coordinates (Fig. 3d) exhibit a region of strong positive correlations ($r_{Ek}^{\sigma_2} > 0.6$) in the upper 500 m spanning the entire Southern Ocean, and in the upper 1 km south of 40°S. This strong correlation between the residual streamfunction in these upper waters and Ekman streamfunction in density coordinates makes sense as these waters are in direct contact with the wind forcing. The strong surface signal of the de-seasoned monthly mean correlations appears to penetrate into the ocean interior along isopycnals from the location of a given σ_2 outcrop a distance of up to 10° of latitude. In the northern region of the Southern Ocean, there is a relatively weaker negative correlation ($r_{Ek}^{\sigma_2} \approx -0.3$) signal, suggesting that on a monthly timescale the residual streamfunction anomalies here are out of phase with those of Ekman streamfunction anomalies. Extending the temporal scale to the 12-month running averages (Fig. 3e) further intensifies the strong correlation ($r_{Ek}^{\sigma_2} > 0.7$) signal of the upper 1 km between 65–40°S. The northward penetration of the strong signal has widened from that of the de-seasoned monthly means to be approximately 15° of latitude in extent. Also, on this annual timescale, the relatively weaker negative signal evident in the de-seasoned monthly means is not longer present, suggesting the variability timescale of this feature is between monthly and annual (i.e., seasonal).

The equivalent scaled regression analysis for the de-seasoned monthly means show that $std\,(\Psi_{Ek}^{\sigma_2}) \cdot \gamma_{Ek}^{\sigma_2}$ is strongest (> 4 Sv) in the upper 1 km between 65–35°S, reaching depths of 2 km for 60–55°S, and with a relatively weaker negative signal (< -2 Sv) to the north between 45–35°S and 1–2.5 km depth (Fig. 3f). The region with the strongest response coincides with the upwelling branch of the "upper cell", or the Atlantic Meridional Overturning Circulation. Widening the temporal scale to the 12-month running averages reduces the breadth of the upper ocean signal, localising the peak to a maximum of $std\,(\Psi_{Ek}^{\sigma_2}) \cdot \gamma_{Ek}^{\sigma_2} > 4$ Sv centered around 52°S and $\sigma_2 = 36\,\text{kg/m}^3$ (Fig. 3g). Note that this location in latitude–potential density space corresponds to the respective maxima of both Ekman streamfunctions; that is, this location is where the wind stress curl changes sign, which has been identified as a region that is particularly sensitive to atmospheric variability, and a hotspot for heat uptake (Stewart & Hogg, 2019).

5 Conclusions

We have introduced a novel wind-derived metric to quantify the variability of the Southern Ocean overturning circulation (SOOC), which we call the Ekman streamfunction. The Ekman streamfunction is developed by integrating the vertical Ekman pumping velocities zonally and northwards from the Antarctic coastline to a given latitude, returning a theoretical representation of the SOOC at the base of the surface Ekman layer. We evaluate the utility of the Ekman streamfunction by way of a global 0.1° ocean–sea-ice model, driven with interannual forcing. The results presented here highlight the close association of the Ekman streamfunction and the SOOC, and the regions and timescales where the two are directly relatable. The covariance between the Ekman streamfunction and the diagnosed SOOC is remarkable; for instance, in regions south of 40°S, and in particular the upwelling flank of Deacon cell, the correlation is greater than 0.9. A scaled regression analysis indicates that for certain locations a one standard deviation change in the Ekman streamfunction coincides with a $> 4\,\mathrm{Sv}$ change in the SOOC on monthly and annual timescales, which amounts to approximately 10% of the Eulerian overturning circulation. The correlation between the residual streamfunction and the Ekman streamfunction in density coordinates penetrates northwards along isopycnals up to 15° of latitude within a year. The scaled regression signal peak at 52°S and $\sigma_2 = 36\,\mathrm{kg/m^3}$, which is the location of the zero wind stress curl, reflects the heightened sensitivity of this specific region to atmospheric variability. The results also suggest that for regions with weak or insignificant correlations, the overturning circulation variability is due to dynamical processes other than wind forcing, such as buoyancy fluxes. In summary, this analysis clearly demonstrates the utility of the novel Ekman streamfunction in representing the wind-driven variability of the SOOC.

Acknowledgments

We acknowledge the support of this work from the Earth Systems and Climate Change Hub funded by the Australian Government's National Environmental Science Program (NESP). Many thanks to Navid Constantinou, Ryan Holmes, Adele Morrison and Jan Zika for very helpful discussions, and to the COSIMA consortium (www.cosima.org.au) for making available the ACCESS-OM2 suite of models. The numerical simulations and analysis were performed with the resources of the National Computational Infrastructure (Canberra, Australia). The ACCESS-OM2 model output is hosted in the COSIMA Model Output Collection: doi:10.4225/41/5a2dc8543105a.

References

Abernathey, R., Marshall, J., & Ferreira, D. (2011). The dependence of Southern Ocean meridional overturning and wind stress. *Journal of Physical Oceanography*, *41*, 2261–2278. doi: 10.1175/JPO-D-11-023.1

Farneti, R., Downes, S., Griffies, S., Marsland, S., Behrens, E., Bentsen, M., ... Yeager, S. (2015). An assessment of Antarctic Circumpolar Current and Southern Ocean meridional overturning circulation during 1958–2007 in a suite of interannual CORE-II simulations. *Ocean Modelling*, *93*, 84–120. doi: 10.1016/j.ocemod.2015.07.009

Goyal, R., Sen Gupta, A., Jucker, M., & England, M. (2021). Historical and projected changes in the Southern Hemisphere surface westerlies. *Geophysical Research Letters*, *48*, e2020GL090849. doi: 10.1029/2020GL090849

Gray, A., & Riser, S. (2014). A global analysis of Sverdrup balance using absolute geostrophic velocities from Argo. *Journal of Physical Oceanography*, *44*, 1213–1229. doi: 10.1175/JPO-D-12-0206.1

Kiss, A., Hogg, A., Hannah, N., Dias, F., Brassington, G., Chamberlain, M., ... Zhang, X. (2020). ACCESS-OM2: A Global Ocean–Sea-Ice Model at

Three Resolutions. *Geoscientific Model Development*, *13*, 401–442. doi: 10.5194/gmd-13-401-2020

Locarnini, R., Mishonov, A., Antonov, J., Boyer, T., Garcia, H., Baranova, O., ... Seidov, D. (2013). World Ocean Atlas 2013, Volume 1: Temperature. *NOAA Atlas NESDIS*, *73*.

Marshall, G. (2003). Trends in the Southern Annular Mode from observations and reanalyses. *Journal of Climate*, *16*, 4134–4143. doi: 10.1175/1520-0442(2003)016⟨4134:TITSAM⟩2.0.CO;2

Marshall, J., & Speer, K. (2012). Closure of the meridional overturning circulation through Southern Ocean upwelling. *Nature Geoscience*, *5*, 171–180. doi: 10.1038/NGEO1391

Roemmich, D., Church, J., Gilson, J., Monselesan, D., Sutton, P., & Wijffels, S. (2015). Unabated planetary warming and its ocean structure since 2006. *Nature Climate Change*, *5*, 240–245. doi: 10.1038/nclimate2513

Sabine, C., Feely, R., Gruber, N., Key, R., Lee, K., Bullister, J., ... Rios, A. (2004). The Oceanic Sink for Anthropogenic CO_2. *Science*, *305*, 367–371. doi: 10.1126/science.1097403

Sallèe, J. (2018). Southern Ocean warming. *Oceanography*, *32*, 52–62. doi: 10.5670/oceanog.2018.215

Sallèe, J., Speer, K., & Rintoul, S. (2010). Zonally asymmetric response of the Southern Ocean mixed-layer depth to the Southern Annular Mode. *Nature Geoscience*, *3*, 273–279. doi: 10.1038/NGEO812

Santer, B., Wigley, T., Boyle, J., Gaffen, D., Hnilo, J., Nychka, D., ... Taylor, K. (2000). Statistical significance of trends and trend differences in layer-average atmospheric temperature time series. *Journal of Geophysical Research: Atmospheres*, *105*, 7337–7356. doi: 10.1029/1999JD901105

Sen Gupta, A., & England, M. (2006). Coupled Ocean–Atmosphere–Ice Response to Variations in the Southern Annular Mode. *Journal of Climate*, *19*, 4457–4485. doi: 10.1175/JCLI3843.1

Stewart, K., & Hogg, A. (2019). Southern Ocean heat and momentum uptake are sensitive to the vertical resolution at the ocean surface. *Ocean Modelling*, *143*, 101456. doi: 10.1016/j.ocemod.2019.101456

Swart, N., & Fyfe, J. (2012). Observed and simulated changes in the Southern Hemisphere surface westerly wind-stress. *Geophysical Research Letters*, *39*, L16711. doi: 10.1029/2012GL052810

Tandon, N., Saenko, O., Cane, M., & Kushner, P. (2020). Interannual variability of the global meridional overturning circulation dominated by pacific variability. *Journal of Physical Oceanography*, *50*, 559–574. doi: 10.1175/JPO-D-19-0129.1

Tsujino, H., Urakawa, S., Griffies, S., Danabasoglu, G., Adcroft, A., Amaral, A., ... Yu, Z. (2020). Evaluation of global ocean–sea-ice model simulations based on the experimental protocols of the Ocean Model Intercomparison Project phase 2 (OMIP-2). *Geoscientific Model Development*, *13*, 3643–3708. doi: 10.5194/gmd-13-3643-2020

Tsujino, H., Urakawa, S., Nakano, H., Small, R., Kim, W., Yeager, S., ... Yamazaki, D. (2018). JRA-55 based surface dataset for driving ocean–sea-ice models (JRA55-do). *Ocean Modelling*, *130*, 79–139. doi: 10.1016/j.ocemod.2018.07.002

Zika, J., England, M., & Sijp, W. (2012). The Ocean Circulation in Thermohaline Coordinates. *Journal of Physical Oceanography*, *42*, 708–724. doi: 10.1175/JPO-D-11-0139.1

Zweng, M., Reagan, J., Antonov, J., Locarnini, R., Mishonov, A., Boyer, T., ... Biddle, M. (2013). World Ocean Atlas 2013, Volume 2: Salinity. *NOAA Atlas NESDIS*, *74*.